Article

Porous Amorphous Silicon Hollow Nanoboxes Coated with Reduced Graphene Oxide as Stable Anodes for Sodium-Ion Batteries

Yi Zhang,[‡] Yun-Cheng Tang,[‡] Xin-Tao Li, Hong Liu, Yong Wang, Yi Xu,* and Fei-Hu Du*

Read Online

ACCESS | Metrics & More | Article Recommendations | Supporting Information

ABSTRACT: Amorphous silicon (a-Si), due to its satisfactory theoretical capacity, moderate discharge potential, and abundant reserves, is treated as one of the most prospective materials for the anode of sodium-ion batteries (SIBs). However, the slow Na$^+$ diffusion kinetics, poor electrical conductivity, and rupture-prone structures of a-Si restrict its further development. In this work, a composite (a-Si@rGO) consisting of porous amorphous silicon hollow nanoboxes (a-Si HNBs) and reduced graphene oxide (rGO) is prepared. The a-Si HNBs are synthesized through "sodiothermic reduction" of silica hollow nanoboxes at a relatively low temperature, and the rGO is covered on the surface of the a-Si HNBs by electrostatic interaction. The as-synthesized composite anode applying in SIBs exhibits a high initial discharge capacity of 681.6 mAh g^{-1} at 100 mA g^{-1}, great stability over 2000 cycles at 800 mA g^{-1}, and superior rate performance (261.2, 176.8, 130.3, 98.4, and 73.3 mAh g^{-1} at 100, 400, 800, 1500, and 3000 mA g^{-1}, respectively). The excellent electrochemical properties are ascribed to synergistic action of the porous hollow nanostructure of a-Si and the rGO coating. This research not only offers an innovative synthetic means for the development of a-Si in various fields but also provides a practicable idea for the design of other alloy-type anodes.
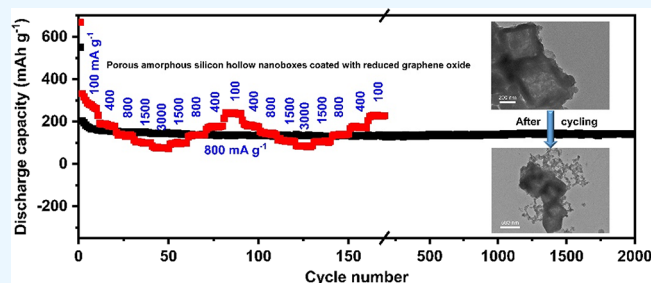
INTRODUCTION

With abundant sodium resource, low cost, and superior power characteristics, sodium-ion batteries (SIBs) are considered to be a promising next-generation secondary battery system for energy storage at scale.[1−4] Designing electrode materials with great specific capacity, robust structure, and good reversibility is a key part of the development of SIBs. Up to now, carbon-based materials with small volume change are still in focus,[5−7] but low theoretical capacities limit their further applications. It has been studied that some materials such as P, Sn, Ge, and Sb[8,9] provide high capacities through alloying reactions. Unfortunately, these materials are highly variable in volume and are likely to crack during the reactions. As for silicon, which is divided into crystalline silicon (c-Si) and amorphous silicon (a-Si), c-Si has received a lot of attention as a lithium-ion battery (LIB) anode due to its highest theoretical lithium storage capacity and low lithium storage potential.[10−14] However, first-principles calculations manifest that the energy requirement for sodium insertion into c-Si is high,[15] which makes the performance of c-Si as an anode for SIBs unsatisfactory. Fortunately, a-Si has an outstanding capacity (0.76 Na atoms per Si, equivalent to 725 mAh g^{-1}), and its volume swelling (∼114%) during the alloying process is much less than that of the alloying materials mentioned above,[16] but its application to the anode of SIBs has been rarely reported. One major issue is the preparation of a-Si, which usually involves expensive (Si targets) or dangerous (SiH$_4$) raw

materials.[17,18] For instance, Huang et al.[17] deposited Si films on a sacrificial layer through electron beam evaporation in vacuum and using Si pellets as a raw material and subsequently removed the sacrificial layer to obtain a rolled-up a-Si nanomembrane anode. In contrast, silica is a cheap and readily available source of Si, and carbothermic reduction and magnesiothermic reduction are two common methods of producing Si from silica. The former uses carbothermic reduction[19] of quartz sand at a high temperature (1900 °C) to produce solar energy Si and the latter originates from magnesiothermic reduction[20] of diatom frustules at a lower temperature (650 °C), but both of these methods yield c-Si. Thus, it can be seen that the production of a-Si from silica is a meaningful task.

Furthermore, the characteristics of a-Si make it difficult to develop.[21,22] First, the slow Na$^+$ transportation increases concentration polarization and adversely affects rate performance. Second, a large swelling rate tends to induce a rapid pulverization of a-Si during electrochemical charge and

discharge and consequently causes fast capacity decay. Finally, the unsatisfactory electrical conductivity of a-Si results in an increased ohmic internal resistance, which is also not conducive to rate performance. To design a high-performance a-Si anode, two strategies are frequently adopted. One is the construction of nanostructures for a-Si.[23,24] For example, Han et al.[23] reported a spongy porous a-Si particle anode with a capacity of 170 mAh g^{-1} after 500 cycles at a current density of 1000 mA g^{-1}. Nanostructures can accommodate volume expansion, shorten the diffusion length of Na$^+$, and facilitate penetration of the electrolyte. The other strategy is to introduce conductive materials.[25−28] Jangid et al.[25] obtained a Si-graphene film anode with an upgraded initial reversible capacity of ∼600 mAh g^{-1} and a capacity of 240 mAh g^{-1} after 100 cycles at 0.1 C, via chemical vapor deposition (CVD) of CH$_4$ on a-Si films. Conductive coatings protect a-Si from direct exposure to the electrolyte, reduce the occurrence of by-reactions, and additionally provide electron transport channels between the collector and the a-Si surface. More importantly, a coating layer with exceptional mechanical ductility can buffer mechanical stress to a certain extent.[29] Although the electrochemical performance of the above a-Si anode has been improved by adding a graphene film through CVD, this method is relatively complex and requires high-temperature equipment. Therefore, it is challenging to explore a simple large-scale synthetic approach for combining nanostructured a-Si and graphene.

Herein, we report a strategy to conveniently fabricate porous amorphous silicon hollow nanoboxes (a-Si HNBs) coated with reduced graphene oxide (rGO), where the key techniques are the sodiothermic reduction of silica hollow nanoboxes (SiO$_2$ HNBs) at a low temperature (450 °C) and in situ wrapping of rGO by electrostatic interaction.[30,31] The obtained composite as an anode of SIBs is found to have remarkably high rate performance and ultralong cycle life, which benefit from two advantages: (i) the porous hollow nanostructure of a-Si that inhibits volume expansion, enhances Na$^+$ diffusion rate, and accelerates electrolyte penetration and (ii) the rGO coating to offer exceptional electrical conductivity, form a steady solid electrolyte interphase (SEI), and buffer the mechanical stress. The project we designed allows both of these strengths to work well together.

■ RESULTS AND DISCUSSION

The preparation process of a-Si@rGO composite is presented in Figure 1. First, SiO$_2$ HNBs were produced according to the universal template method, and Fe$_2$O$_3$ nanocubes were used as sacrificial templates and chemically coated with SiO$_2$, followed by etching the Fe$_2$O$_3$ with HCl to obtain the SiO$_2$ HNBs. Second, a-Si HNBs were formed by sodiothermic reduction of the SiO$_2$ HNBs under vacuum and 450 °C. After that, 3-aminopropyltriethoxysilane (APTES) was employed to introduce positive charges on the surface of the a-Si HNBs, and the doublet peaks between 3300 and 3500 cm^{-1} in the Fourier transform infrared (FT-IR) spectra of the treated a-Si HNBs (Figure S1) confirm the efficacious modification of amino groups on the a-Si HNBs,[32] and then, the positively charged a-Si HNBs and negatively charged graphene oxide (GO) were assembled by electrostatic interaction. At last, a-Si@rGO composite was fabricated by chemical reduction with the addition of hydrazine.

The morphology and structure of the products (Figure 2) were observed via a scanning electron microscope (SEM) and
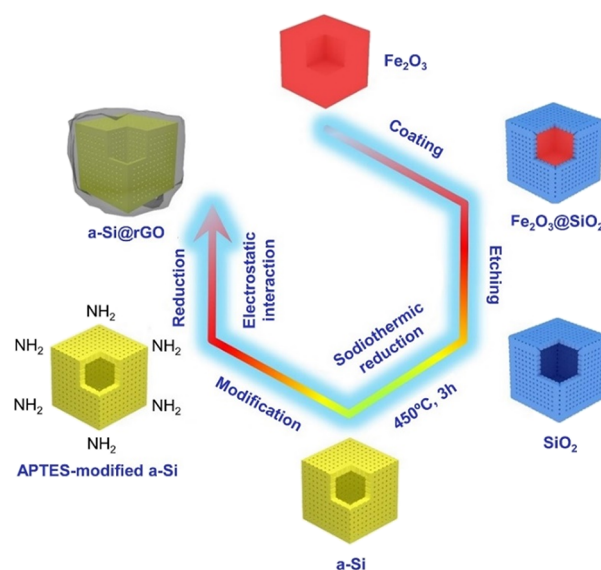

Figure 1. Schematic illustration of the fabrication method of the a-Si@rGO composite.

a transmission electron microscope (TEM). The SEM image indicates that the SiO$_2$ maintains a uniform cube shape with a prism length of ∼300 nm (Figure 2a), and the TEM photograph illustrates the hollow state of the SiO$_2$ with a wall width of ∼45 nm (Figure 2d). After removal of the red Fe$_2$O$_3$ nanocubes, the white SiO$_2$ HNBs were gained (Figure S2a,b). Apparently, a-Si inherits a cube shape after the sodiothermic reduction and acid treatment (Figure 2b,e). In addition to that, Figure 2e shows that the a-Si has a rough shell with slight expansion, while the hollow structure is totally preserved. As the result of the strong electrostatic interaction, the a-Si HNBs are tightly coated by the rGO sheets (Figure 2c,f). Crinkled surfaces are created due to the presence of the rGO, and it is noteworthy that the adjacent a-Si HNBs are connected by the flexible rGO (Figure 2c). The ultrathin nature of the rGO sheets can be confirmed from Figure 2f, where individuals along with overlapping rGO layers at the edge of the a-Si HNBs are clearly observed. In addition, after the rGO coating treatment, the brown a-Si HNBs turns into the black a-Si@rGO composite (Figure S2c,d).

The X-ray diffraction (XRD) spectra of the products are shown in Figure 3a. There is a broad peak at 23° for the a-Si HNBs and no reflection peaks of c-Si can be detected, evincing the amorphous nature of Si. After the coating treatment, the XRD pattern of the a-Si@rGO composite displays the absence of the graphene (002) peak because of the lack of substantial stacking of the rGO sheets. The Raman spectrum of the a-Si HNBs (inset of Figure 3b) shows an evident peak at 470 cm^{-1}, correlating with a-Si vibration modes.[33,34] However, it is relatively weak for the a-Si Raman peak in the a-Si@rGO composite (Figure 3b), pointing to the complete wrapping of the rGO sheets on the a-Si HNBs. Notably, the peak of a-Si is slightly shifted to the right, which may be the result of the interaction between the a-Si HNBs and the rGO. In addition, the two intense peaks at 1342 and 1596 cm^{-1} are designated as the disordered D peak and the graphitized G peak of the rGO, respectively. To further demonstrate the successful synthesis of the a-Si HNBs, the Si 2p XPS spectrum (Figure 3c) was inspected. The dominant peak at 99.7 eV is responsible for the Si−Si bond and the comparatively weak peak at 103.4 eV
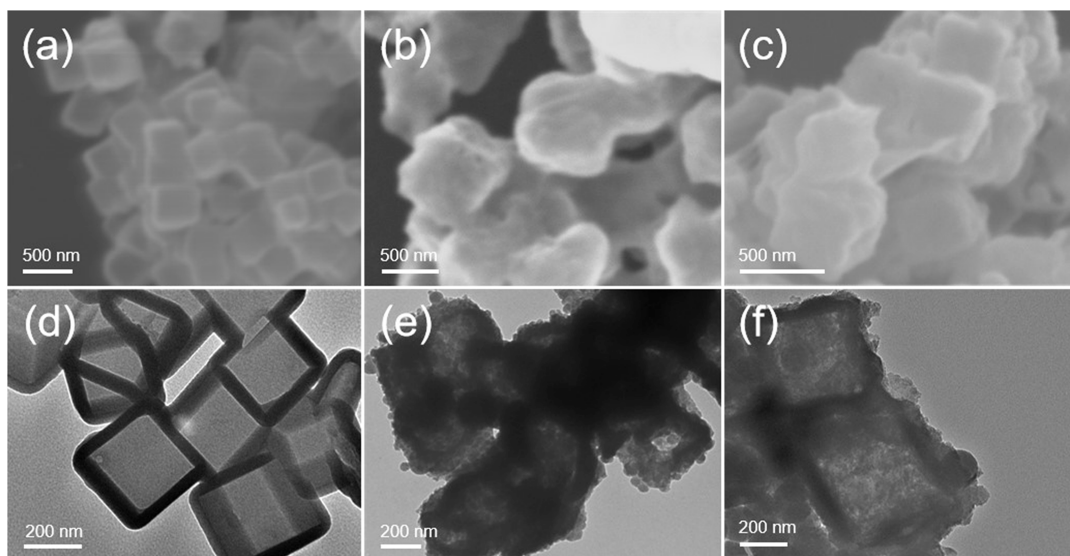
Figure 2. Morphological and structural characterization of the materials: (a−c) SEM images of (a) the SiO$_2$ HNBs, (b) a-Si HNBs, and (c) a-Si@rGO composite. (d−f) TEM images of (d) the SiO$_2$ HNBs, (e) a-Si HNBs, and (f) a-Si@rGO composite.
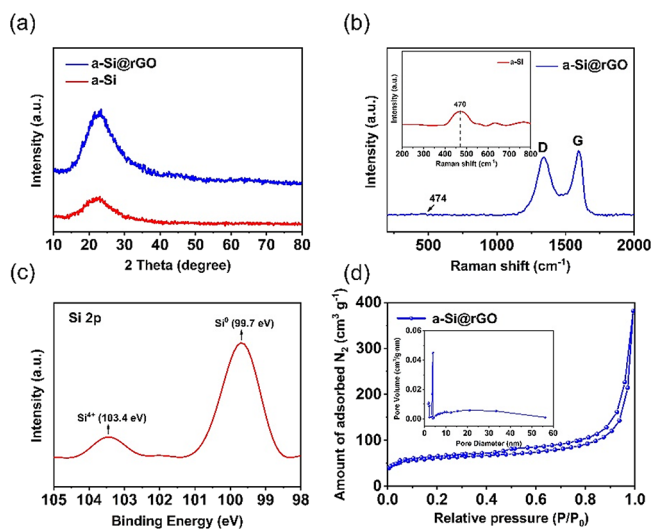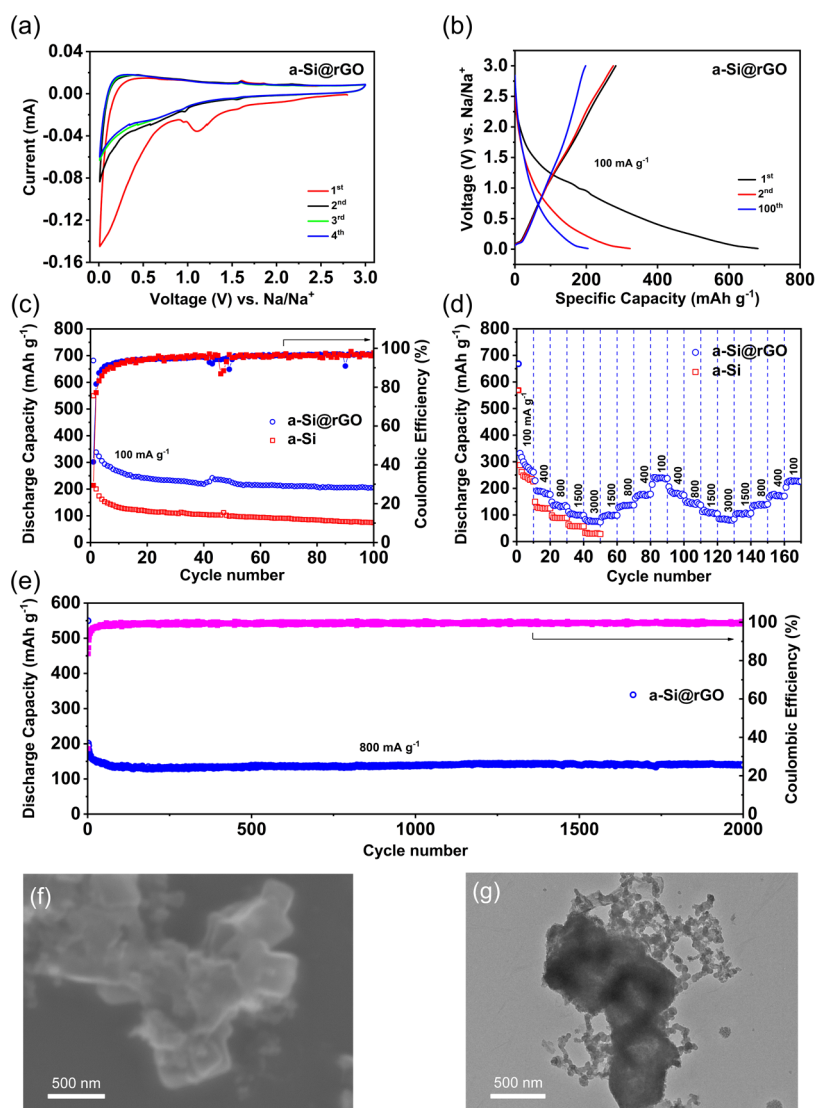

Figure 3. (a) XRD patterns of the a-Si@rGO composite and a-Si HNBs. (b) Raman spectra of the a-Si@rGO composite and a-Si HNBs (inset). (c) Si 2p XPS spectrum of the a-Si HNBs. (d) N$_2$ adsorption−desorption isotherms and pore size distribution (inset) of the a-Si@rGO composite.

belongs to the Si−O bond,[23] suggesting that a small amount of SiO$_2$ may be generated during the preparation of the material. The Brunauer−Emmett−Teller (BET) surface area (Figure 3d and Figure S3) of the a-Si@rGO composite (199 m^2 g^{-1}) is bigger than that of the a-Si HNBs (178 m^2 g^{-1}), resulting from the low density of the rGO.[35] Additionally, the Barrett−Joyner−Halenda (BJH) pore size of the a-Si@rGO composite (21.56 nm) is larger than that of the a-Si HNBs (6.77 nm), indicating that extra pores are created since the interlinking of the rGO, which is consistent with the previous report.[36] The calculated contents of a-Si and rGO in the a-Si@rGO composite (Figure S4) are 95.5 and 4.5 wt % as estimated by thermogravimetric analysis (TGA), respectively, meaning a high utilization of a-Si in the composite.

Figure 4a presents the cyclic voltammogram (CV) curves of the a-Si@rGO composite at a scan rate of 0.1 mV s^{-1}. In the cathodic process, an irreversible peak emerges at around 1.1 V in the first cycle and vanishes completely in the subsequent cycles, which may be related to SEI film formation and oxide layer reduction. The broad peaks locating at ~0.58 V from the second cycle onward correspond to sodium uptake in a-Si. In the anodic process, the desodiation happens in a voltage range of 0.25−1.0 V. These characteristics are matched with those described in the literature.[37] The galvanostatic charge/discharge profiles of the a-Si@rGO composite electrode at the 1st, 2nd, and 100th cycles with a current density of 100 mA g^{-1} are displayed in Figure 4b. During the first discharge course, a voltage plateau that occurs at ~1.2 V is assigned to the generation of the SEI layer. Afterward, a long sloping lower plateau below 0.7 V represents the Na$^+$ insertion into a-Si. Moreover, the initial charge/discharge capacities of the a-Si@rGO composite electrode are 282.9 and 681.6 mAh g^{-1}, respectively. Actually, the capacity loss is the consequence of the irreversible insertion of Na$^+$ into a-Si and the generation of the SEI film on the composite surface caused by electrolyte decomposition.

As revealed in Figure 4c, the comparison of cycling stability between the a-Si@rGO composite and a-Si HNBs was performed at a current density of 100 mA g^{-1}. The discharge capacity of the pure a-Si HNBs electrode at the 100th cycle is 83.5 mAh g^{-1}, and the capacity retention is merely 37% in comparison with that of the 2nd cycle. By contrast, the a-Si@rGO composite electrode exhibits an improved stability with a capacity of 204.8 mAh g^{-1} for the 100th cycle and the capacity retention is 60% compared to the 2nd cycle. In addition to this, the long-term cycling behavior of the a-Si@rGO composite electrode was analyzed at 800 mA g^{-1} (Figure 4e). The discharge capacity of the composite electrode after 2000 cycles is 142.1 mAh g^{-1}, which corresponds to 71% of its capacity at the 2nd cycle. High Coulombic efficiencies of >95% are consistently maintained after 10 cycles. Meanwhile, the rGO electrode displays a far lower capacity (Figure S5) than the a-Si@rGO composite electrode, demonstrating that most of the sodium storage capacity of the composite is provided by a-Si. Synergistic effect can explain the outstanding cycle performance of the a-Si@rGO composite electrode. The porous hollow

Figure 4. (a) CV curves and (b) galvanostatic charge/discharge profiles of the a-Si@rGO composite. (c) Comparisons of cycling stability and CEs between the a-Si@rGO composite and a-Si HNBs at a low current density of 100 mA g^{-1}. (d) Rate capability of the a-Si@rGO composite and a-Si HNBs. (e) Long-term cycling performance and CEs of the a-Si@rGO composite at a current density of 800 mA g^{-1}. (f) SEM and (g) TEM images of the a-Si@rGO composite after 50 cycles at various current densities (100−3000 mA g^{-1}).

nanostructure of a-Si can offer a space for volume expansion and decrease diffusion-induced stress. The rGO coating can partially restrain volume swelling, decrease the direct contact between the a-Si HNBs and electrolyte, and form a durable SEI layer on the composite surface.

Figure 4d shows the rate capability of the a-Si@rGO composite and a-Si HNB electrodes at different current densities of 100−3000 mA g^{-1}. The capacities of the a-Si HNB electrode are 226.1, 124.6, 89.3, 57.1, and 28.3 mAh g^{-1} at 100, 400, 800, 1500, and 3000 mA g^{-1}, respectively. For the a-Si@rGO composite electrode, higher discharge capacities of 261.2, 176.8, 130.3, 98.4, and 73.3 mAh g^{-1} are reached at corresponding current densities. Moreover, a high discharge capacity of 214.7 mAh g^{-1} is regained as the current density is adjusted from 3000 to 100 mA g^{-1}. In the later cycling periods, the a-Si@rGO composite electrode still keeps acceptable discharge capacities, proving the significantly boosted rate performance. The remarkable rate capability of the composite is based on the following factors. On the one hand, the porous channels and hollow structure of a-Si accelerate ion diffusion

and electrolyte penetration, ensuring rapid Na$^+$ insertion and extraction. On the other hand, the rGO shell promotes the electrical conductivity effectively, delivering an efficient electron transport pathway between the composite and the collector. In order to verify the structural integrity, the SEM and TEM images of the a-Si@rGO composite after cycling at various current densities were observed (Figure 4f,g). The cube shape, as well as hollow structure, is highly maintained, which validates the importance of the enhanced electrode integrity for excellent rate performance.

Studying the kinetic behavior of the a-Si@rGO composite is an important way to ascertain the charge storage mechanism, for which the CV curves were researched in a scan rate range of 0.1−1.0 mV s^{-1} (Figure 5a). These curves present similar shapes of broad peaks and low polarized voltage, suggesting high reversibility of the a-Si@rGO composite electrode. In addition, the charge storage was simulated by the known relationship between the current (i) and scan rate (v) basing on the power law equation:[38]
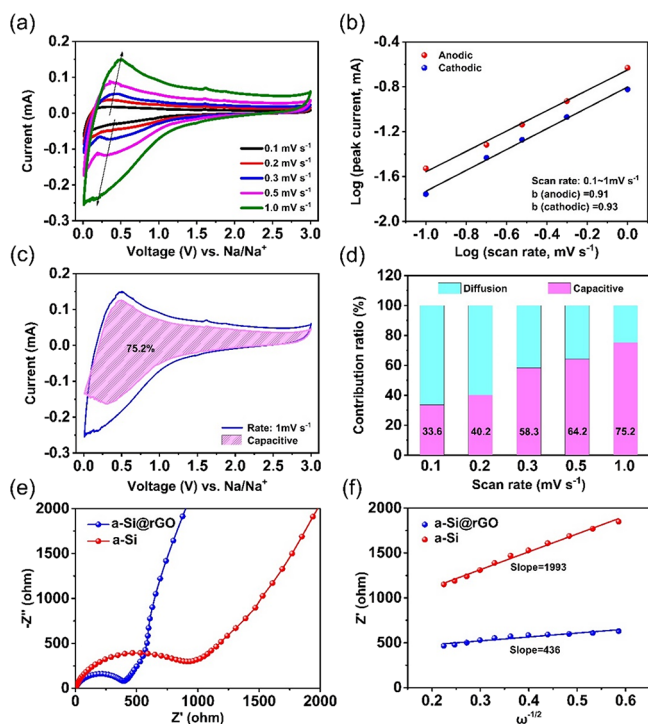
Figure 5. Kinetic analysis: (a) CV curves of the a-Si@rGO composite at various scan rates of 0.1−1.0 mV s^{-1}. (b) b-values of the cathodic and anodic peaks. (c) Segregation of the capacitive and diffusion currents at 1.0 mV s^{-1}. (d) Contribution ratio chart of capacitive and diffusion-controlled capacities at different scan rates. (e) Nyquist plots of the a-Si@rGO composite and a-Si HNBs after the 100th cycle at 100 mA g^{-1}. (f) Z′ as a function of the $\omega^{-1/2}$ plot in the low frequency range (the slope of fitting lines is the Warburg factor, σ_ω).

$$i_{(V)} = av^b = k_1v + k_2v^{1/2} \tag{1}$$

The b-value mirrors the charge storage kinetics of the composite material. In general, $b = 0.5$ or $b = 1$ implies the diffusion- or surface-controlled sodium storage processes,[39] respectively. The computed values explain that the electrochemical reactions of the a-Si@rGO composite electrode are primarily dominated by the surface capacitive behavior, because the slopes b of the anode and cathode peaks are 0.91 and 0.93 (Figure 5b), respectively, close to 1.0. Moreover, the capacitance contributions are quantified according to the above equation and divided into capacitive (k_1) and diffusion (k_2)-controlled sections at a constant potential. The fitting data expresses that the ratio of the surface capacitance for the a-Si@rGO composite electrode is up to ∼75.2% at 1.0 mV s^{-1} (Figure 5c), indicating that the kinetic behavior is mainly controlled by the surface capacitive process. The proportion of the capacitive contribution grows with an increasing scan rate (Figure 5d), owing to the fact that a large scan rate can suppress the diffusion of Na$^+$ to some extent.

To distinguish the difference in the charge transfer rate with and without graphene coating, the electrochemical impedance spectroscopy (EIS) of the a-Si@rGO composite and a-Si HNBs was evaluated after the 100th cycle (Figure 5e). The charge transfer impedance of the a-Si@rGO composite electrode (397 Ω) is much lower than that of the a-Si HNBs electrode (911 Ω). This proves that the composite possesses a faster charge transfer process, which can be obviously recognized from the Nyquist plots. Furthermore, the diffusion rate of Na$^+$ can be worked out from the universal equation:[40]

$$D_{(Na^+)} = R^2T^2/(2A^2n^4F^4C^2\sigma_\omega^2) \tag{2}$$

The Warburg coefficients σ_ω of the a-Si@rGO composite and a-Si HNBs (Figure 5f) after 100 cycles are 436 and 1993 Ω s$^{-1/2}$, respectively. Correspondingly, the $D_{(Na^+)}$ values calculated according to the formula are 1.32×10^{-16} and 6.33×10^{-18} cm^2 s^{-1}. Overall, the outcomes suggest that the a-Si@rGO composite can achieve rapid charge transfer and sustain quick Na$^+$ transport during cycling.

■ CONCLUSIONS

In conclusion, the a-Si@rGO composite anode for SIBs has been successfully synthesized via sodiothermic reduction and electrostatic interaction. The composite is cleverly endowed with a porous hollow nanostructure and rGO layer, which exhibits attractive electrochemical performance in terms of sodium storage capacity, cycling stability, and rate capability. The porous hollow nanostructure of a-Si not only accommodates the volume variation but also makes Na$^+$ and electrolyte to diffuse rapidly into the electrode. Meanwhile, the rGO coating partly inhibits the volume expansion of a-Si, prevents the a-Si HNBs from directly contacting the electrolyte, and provides superb electrical conductivity. The rational strategy delivers a novel insight into the low-cost controlled synthesis of a-Si and the large-scale application of high-performance a-Si-based anodes in SIBs.

■ EXPERIMENTAL SECTION

Preparation of Fe$_2$O$_3$ Nanocubes. First, anhydrous iron nitrate (2.242 g) and zinc acetate dihydrate (0.675 g) were dissolved in deionized water (30 mL), and then concentrated ammonia (30 mL) was added and stirred for 60 min. Second, the solution was moved to a PTFE autoclave and kept at 160 °C for 10 h. Finally, Fe$_2$O$_3$ nanocubes were obtained after the filtration and drying processes.

Synthesis of SiO$_2$ HNBs. The as-prepared Fe$_2$O$_3$ nanocubes (0.1 g) were ultrasonically dispersed in an aqueous ethanol solution (ethanol:water = 100 mL:10 mL), and concentrated ammonia (5 mL) was then added in slow drip and stirred for 30 min as solution A. Ethanol (4.5 mL) and ethyl orthosilicate (0.5 mL) were mixed as solution B. Then, solution B was injected to A at a drop rate of 1 mL min^{-1} and stirred for 8 h at 35 °C. After filtering the mixed solution, the residue was dried and calcined at 450 °C for 6 h. Finally, the powder was dispersed in 1 mol/L hydrochloric acid solution with stirring at 90 °C for 48 h to etch Fe$_2$O$_3$, and the SiO$_2$ HNBs were acquired after centrifugation and drying.

Synthesis of Porous a-Si HNBs. In a glovebox, fine lumps of sodium (0.1 g) and the SiO$_2$ HNBs (0.1 g) were mixed in a necked glass tube, which was subsequently encapsulated under vacuum, and then transferred it to a muffle furnace followed by heating to 450 °C at a slow ramp rate of 1 °C min^{-1} and held for 3 h. Afterward, the glass tube was cracked open and the resultant was first soaked in anhydrous ethanol for removing unreacted trace amounts of metal sodium and then in dilute hydrochloric acid for solving sodium oxides. The porous a-Si HNBs were attained by drying the filtrate at 60 °C for 10 h in a vacuum.

Fabrication of a-Si@rGO Composite. The a-Si HNBs (0.25 g) and anhydrous ethanol (40 mL) were mixed in a

three-mouth flask and stirred for 20 min to disperse evenly. Then, the three-mouth flask was placed in an 80 °C water bath, APTES (2.5 mL) was added under an argon atmosphere with constant mechanical stirring, and the reflux procedure was performed at 80 °C for 8 h. Then, the aminated a-Si HNBs were gained after filtration and washed with anhydrous ethanol. The original GO was produced with reference to the modified Hummers method. The aminated a-Si HNBs (70 mg) were dispersed in deionized water (50 mL) and poured into a GO suspension (150 mL, 0.05 mg/mL). After a light magnetic stirring for 1 h, a hydrazine solution (0.5 mL, 35 wt %) was employed for the reduction of GO. The a-Si@rGO composite was collected after washing with deionized water.

Material Characterization. The functional groups were detected by employing a Nicolet 380 Fourier transform infrared (FT-IR) spectroscopy. The morphology and structure of the samples were observed through a JEOL JSM-6700F SEM and a JEOL JEM-2010F TEM. The physical phase was determined using a Rigaku D/max-2550 V X-ray powder diffractometer with a Cu-Kα radiation source. The information about surface chemical composition and state of the samples were given using a Renishaw inVia Microscope Raman spectrometer and a Perkin Elmer PHI ESCA-5000C X-ray photoelectron spectroscopy (XPS) analyzer. The pore size distribution and specific surface area were researched using an ASAP 2010 M + C analyzer. TGA curves were obtained using a NETZSCH STA 409 PG/P thermogravimetric analyzer.

Battery Device Fabrication. Samples, carbon black, and sodium carboxymethyl cellulose (CMC) were evenly mixed in a specific mass ratio (7:2:1), and a suitable amount of deionized water was added to stir into a viscous slurry. The slurry was covered on a washed copper foil collector and immediately dried in a vacuum oven at 60 °C for 10 h to obtain negative electrodes. The copper foil was cut to the proper size as the working electrode, and button cells were assembled in a glovebox with metal sodium as the counter electrode, glass fiber as the separator, and 1 M sodium hexafluorophosphate ($NaPF_6$) in an ethylene carbonate (EC)/ diethyl carbonate (DEC) mixture (1: 1, v/v) containing 2 wt % fluoroethylene carbonate (FEC) as the electrolyte.

Battery Device Characterization. CV were tested at 25 °C on a Tatsuwa CHI 660D electrochemical workstation with voltage limits of 0.01 and 3.0 V. EIS was also evaluated on this equipment. Charge/discharge tests were investigated at 25 °C using the LAND-CT 2001A test system.

■ ASSOCIATED CONTENT

Ⓢ Supporting Information

The Supporting Information is available free of charge at https://pubs.acs.org/doi/10.1021/acsomega.2c03322.

FTIR spectra, physical pictures, N_2 adsorption– desorption isotherms and pore size distribution curves, TGA curves, and cycling performance (PDF)

■ AUTHOR INFORMATION

Corresponding Authors

Yi Xu − School of Environmental and Chemical Engineering, Shanghai University, Shanghai 200444, P. R. China; Email: tree2000xy@shu.edu.cn

Fei-Hu Du − School of Environmental and Chemical Engineering, Shanghai University, Shanghai 200444, P. R. China; ⓘ orcid.org/0000-0001-5498-0700; Email: fh_du@shu.edu.cn

Authors

Yi Zhang − School of Environmental and Chemical Engineering, Shanghai University, Shanghai 200444, P. R. China

Yun-Cheng Tang − School of Environmental and Chemical Engineering, Shanghai University, Shanghai 200444, P. R. China

Xin-Tao Li − School of Environmental and Chemical Engineering, Shanghai University, Shanghai 200444, P. R. China

Hong Liu − School of Environmental and Chemical Engineering, Shanghai University, Shanghai 200444, P. R. China; ⓘ orcid.org/0000-0002-4926-1960

Yong Wang − School of Environmental and Chemical Engineering, Shanghai University, Shanghai 200444, P. R. China; ⓘ orcid.org/0000-0003-3489-7672

Complete contact information is available at:
https://pubs.acs.org/10.1021/acsomega.2c03322

Author Contributions

[‡]Y.Z. and Y.C.T. contributed equally to this work.

Notes

The authors declare no competing financial interest.

■ ACKNOWLEDGMENTS

■ REFERENCES

(1) Nayak, P. K.; Yang, L.; Brehm, W.; Adelhelm, P. From lithium-ion to sodium-ion batteries: advantages, challenges, and surprises. Angew. Chem., Int. Ed. 2018, 57, 102−120.

(2) Delmas, C. Sodium and sodium-ion batteries: 50 years of research. Adv. Energy Mater. 2018, 8, 1703137.

(3) Pu, X.; Wang, H.; Zhao, D.; Yang, H.; Ai, X.; Cao, S.; Chen, Z.; Cao, Y. Recent progress in rechargeable sodium-ion batteries: toward high-power applications. Small 2019, 15, 1805427.

(4) Kubota, K.; Dahbi, M.; Hosaka, T.; Kumakura, S.; Komaba, S. Towards K-ion and Na-ion batteries as "beyond Li-ion". Chem. Rec. 2018, 18, 459−479.

(5) Balogun, M. S.; Luo, Y.; Qiu, W.; Liu, P.; Tong, Y. A review of carbon materials and their composites with alloy metals for sodium ion battery anodes. Carbon 2016, 98, 162−178.

(6) Wasalathilake, K. C.; Li, H.; Xu, L.; Yan, C. Recent advances in graphene based materials as anode materials in sodium-ion batteries. J. Energy Chem. 2020, 42, 91−107.

(7) Xiao, L.; Cao, Y.; Henderson, W. A.; Sushko, M. L.; Shao, Y.; Xiao, J.; Wang, W.; Engelhard, M. H.; Nie, Z.; Liu, J. Hard carbon nanoparticles as high-capacity, high-stability anodic materials for Na-ion batteries. Nano Energy 2016, 19, 279−288.

(8) Guo, S.; Feng, Y.; Wang, L.; Jiang, Y.; Yu, Y.; Hu, X. Architectural engineering achieves high-performance alloying anodes for lithium and sodium ion batteries. Small 2021, 17, 2005248.

(9) Fang, L.; Bahlawane, N.; Sun, W.; Pan, H.; Xu, B. B.; Yan, M.; Jiang, Y. Conversion-alloying anode materials for sodium ion batteries. Small 2021, 17, 2101137.

(10) Du, F. H.; Wang, K. X.; Chen, J. S. Strategies to succeed in improving the lithium-ion storage properties of silicon nanomaterials. J. Mater. Chem. A 2016, 4, 32−50.

(11) An, W.; Gao, B.; Mei, S.; Xiang, B.; Fu, J.; Wang, L.; Zhang, Q.; Chu, P. K.; Huo, K. Scalable synthesis of ant-nest-like bulk porous silicon for high-performance lithium-ion battery anodes. *Nat. Commun.* **2019**, *10*, 1447.

(12) Du, F. H.; Ni, Y.; Wang, Y.; Wang, D.; Ge, Q.; Chen, S.; Yang, H. Y. Green fabrication of silkworm cocoon-like silicon-based composite for high-performance Li-ion batteries. *ACS Nano* **2017**, *11*, 8628−8635.

(13) Qu, F.; Li, C.; Wang, Z.; Strunk, H. P.; Maier, J. Metal-induced crystallization of highly corrugated silicon thick films as potential anodes for Li-ion batteries. *ACS Appl. Mater. Interfaces* **2014**, *6*, 8782−8788.

(14) Qu, F.; Li, C.; Wang, Z.; Wen, Y.; Richter, G.; Strunk, H. P. Eutectic nano-droplet template injection into bulk silicon to construct porous frameworks with concomitant conformal coating as anodes for Li-ion Batteries. *Sci. Rep.* **2015**, *5*, 10381.

(15) Legrain, F.; Malyi, O. I.; Manzhos, S. Comparative computational study of the energetics of Li, Na, and Mg storage in amorphous and crystalline silicon. *Comput. Mater. Sci.* **2014**, *94*, 214−217.

(16) Lim, C. H.; Huang, T. Y.; Shao, P. S.; Chien, J. H.; Weng, Y. T.; Huang, H. F.; Hwang, B. J.; Wu, N. L. Experimental study on sodiation of amorphous silicon for use as sodium-ion battery anode. *Electrochim. Acta* **2016**, *211*, 265−272.

(17) Huang, S.; Liu, L.; Zheng, Y.; Wang, Y.; Kong, D.; Zhang, Y.; Shi, Y.; Zhang, L.; Schmidt, O. G.; Yang, H. Y. Efficient sodium storage in rolled-up amorphous Si nanomembranes. *Adv. Mater.* **2018**, *30*, 1706637.

(18) Wang, F.; Zhang, X.; Hong, R.; Lu, X.; Zhu, Y.; Zheng, Y. High-performance anode of lithium ion batteries with plasma-prepared silicon nanoparticles and a three-component binder. *Electrochim. Acta* **2021**, *390*, No. 138809.

(19) Cherif, F.; Ahmed, I. B.; Abderrahmane, A.; Hamzaoui, S. Effect of pellet size and additive on silica carbothermic reduction in microwave furnace for solar grade silicon. *Mater. Sci.-Pol.* **2019**, *37*, 122−126.

(20) Bao, Z.; Weatherspoon, M. R.; Shian, S.; Cai, Y.; Graham, P. D.; Allan, S. M.; Ahmad, G.; Dickerson, M. B.; Church, B. C.; Kang, Z.; Abernathy, H. W., III; Summers, C. J.; Liu, M.; Sandhage, K. H. Chemical reduction of three-dimensional silica micro-assemblies into microporous silicon replicas. *Nature* **2007**, *446*, 172−175.

(21) Jung, S. C.; Jung, D. S.; Choi, J. W.; Han, Y. K. Atom-level understanding of the sodiation process in silicon anode material. *J. Phys. Chem. Lett.* **2014**, *5*, 1283−1288.

(22) Cui, Z.; Li, C.; Yu, P.; Yang, M.; Guo, X.; Yin, C. Reaction pathway and wiring network dependent Li/Na storage of micro-sized conversion anode with mesoporosity and metallic conductivity. *J. Mater. Chem. A* **2015**, *3*, 509−514.

(23) Han, Y.; Lin, N.; Xu, T.; Li, T.; Tian, J.; Zhu, Y.; Qian, Y. An amorphous Si material with a sponge-like structure as an anode for Li-ion and Na-ion batteries. *Nanoscale* **2018**, *10*, 3153−3158.

(24) Du, F. H.; Zhang, L.; Tang, Y. C.; Li, S. Q.; Huang, Y.; Dong, L.; Li, Q.; Liu, H.; Wang, D.; Wang, Y. Low-temperature synthesis of amorphous silicon and its ball-in-ball hollow nanospheres as high-performance anodes for sodium-ion batteries. *Adv. Mater. Interfaces* **2022**, *9*, 2102158.

(25) Jangid, M. K.; Vemulapally, A.; Sonia, F. J.; Aslam, M.; Mukhopadhyay, A. Feasibility of reversible electrochemical Na-storage and cyclic stability of amorphous silicon and silicon-graphene film electrodes. *J. Electrochem. Soc.* **2017**, *164*, A2559−A2565.

(26) Zhao, Q. J.; Huang, Y. H.; Hu, X. L. A Si/C nanocomposite anode by ball milling for highly reversible sodium storage. *Electrochem. Commun.* **2016**, *70*, 8−12.

(27) Du, F. H.; Li, B.; Fu, W.; Xiong, Y. J.; Wang, K. X.; Chen, J. S. Surface binding of polypyrrole on porous silicon hollow nanospheres for Li-ion battery anodes with high structure stability. *Adv. Mater.* **2014**, *26*, 6145−6150.

(28) Wang, P.; Tian, J.; Hu, J.; Zhou, X.; Li, C. Supernormal conversion anode consisting of high-density MoS₂ bubbles wrapped in thin carbon network by self-sulfuration of polyoxometalate complex. *ACS Nano* **2017**, *11*, 7390−7400.

(29) Pramudita, J. C.; Pontiroli, D.; Magnani, G.; Gaboardi, M.; Ricco, M.; Milanese, C.; Brand, H. E. A.; Sharma, N. Graphene and selected derivatives as negative electrodes in sodium- and lithium-ion batteries. *ChemElectroChem* **2015**, *2*, 600−610.

(30) Yang, S.; Feng, X.; Ivanovici, S.; Mullen, K. Fabrication of graphene-encapsulated oxide nanoparticles: towards high-performance anode materials for lithium storage. *Angew. Chem., Int. Ed.* **2010**, *49*, 8408−8411.

(31) Xie, J.; Zhang, Y.; Han, Y.; Li, C. High-capacity molecular scale conversion anode enabled by hybridizing cluster-type framework of high loading with amino-functionalized graphene. *ACS Nano* **2016**, *10*, 5304−5313.

(32) Goller, M. I.; Barthet, C.; McCarthy, G. P.; Corradi, R.; Newby, B. P.; Wilson, S. A.; Armes, S. P.; Luk, S. Y. Synthesis and characterization of surface-aminated polypyrrole-silica nanocomposites. *Colloid Polym. Sci.* **1998**, *276*, 1010−1018.

(33) Deng, J.; Ji, H.; Yan, C.; Zhang, J.; Si, W.; Baunack, S.; Oswald, S.; Mei, Y.; Schmidt, O. G. Naturally rolled-up C/Si/C trilayer nanomembranes as stable anodes for lithium-ion batteries with remarkable cycling performance. *Angew. Chem., Int. Ed.* **2013**, *52*, 2326−2330.

(34) Miyazaki, R.; Ohta, N.; Ohnishi, T.; Sakaguchi, I.; Takada, K. An amorphous Si film anode for all-solid-state lithium batteries. *J. Power Sources* **2014**, *272*, 541−545.

(35) Guo, M.; Zhong, S.; Xu, T.; Huang, Y.; Xia, G.; Zhang, T.; Yu, X. 3D hollow MXene (Ti₃C₂)/reduced graphene oxide hybrid nanospheres for high-performance Li-ion storage. *J. Mater. Chem. A* **2021**, *9*, 23841−23849.

(36) Yang, J.; Voiry, D.; Ahn, S. J.; Kang, D.; Kim, A. Y.; Chhowalla, M.; Shin, H. S. Two-dimensional hybrid nanosheets of tungsten disulfide and reduced graphene oxide as catalysts for enhanced hydrogen evolution. *Angew. Chem., Int. Ed.* **2013**, *52*, 13751−13754.

(37) Xu, Y.; Swaans, E.; Basak, S.; Zandbergen, H. W.; Borsa, D. M.; Mulder, F. M. Reversible Na-ion uptake in Si nanoparticles. *Adv. Energy Mater.* **2016**, *6*, 1501436.

(38) Fleischmann, S.; Mitchell, J. B.; Wang, R.; Zhan, C.; Jiang, D. E.; Presser, V.; Augustyn, V. Pseudocapacitance: from fundamental understanding to high power energy storage materials. *Chem. Rev.* **2020**, *120*, 6738−6782.

(39) Zhang, H.; Sun, W.; Chen, X.; Wang, Y. Few-layered fluorinated triazine-based covalent organic nanosheets for high-performance alkali organic batteries. *ACS Nano* **2019**, *13*, 14252−14261.

(40) Zhang, S.; Zeng, Y.; Wang, Z.; Zhao, J.; Dong, G. Glycerol-controlled synthesis of MoS₂ hierarchical architectures with well-tailored subunits and enhanced electrochemical performance for lithium ion batteries. *Chem. Eng. J.* **2018**, *334*, 487−496.